


Hierarchy among the crystal lattice, charge density wave, and superconducting orders in transition metal dichalcogenides

Valeri Petkov^{1,*}, Junjie Yang², Sarvjit Shastri³, and Yang Ren³

¹*Department of Physics, Central Michigan University, Mt. Pleasant, Michigan 48858, USA*

²*Department of Physics, New Jersey Institute of Technology, Newark, New Jersey 07102, USA*

³*X-ray Science Division, Advanced Photon Source, Argonne National Laboratory, Argonne, Illinois 60439, USA*

 (Received 13 June 2020; revised 22 September 2020; accepted 22 September 2020; published 29 October 2020)

Using high-energy x-ray scattering and large-scale three-dimensional (3D) structure modeling, we investigate the relationship between the crystal lattice, charge density wave (CDW), and superconducting (SC) orders in transition metal dichalcogenides (TMDs). In particular, we systematically substitute Te for Se in Ta-Se-Te solid solutions, determine changes in their crystal lattice, and relate them to changes in the CDW transition temperature, T_{CDW} , and SC critical temperature, T_c . We find that strong lattice distortions such as buckling of Ta layers are detrimental to the CDW and SC orders. The presence of a perfect lattice order in two dimensions is a prerequisite to the emergence of CDWs but insufficient to achieve a SC ordered state. For the SC order to emerge, the Ta sublattice should also appear periodic in 3D. Local chemical disorder may promote the SC order, and the perfectness of Ta coordination polyhedra is a factor contributing to its strength. A hierarchical relationship among the crystal lattice, CDW, and SC orders thus appears to exist in TMDs in a sense that different degrees of crystal lattice order-disorder promote and maintain the CDW and SC orders to a different extent, offering an opportunity to control the latter through modifying the former by rational design. Our findings are a step towards a better understanding of the correlation between lattice and electronic degrees of freedom in TMDs. We also demonstrate an efficient experimental approach to study them in fine detail.

DOI: [10.1103/PhysRevB.102.134119](https://doi.org/10.1103/PhysRevB.102.134119)

I. INTRODUCTION

Layered transition metal dichalcogenides (TMDs) exhibit a variety of lattice structures and collective electronic states, including charge density waves (CDWs) and superconducting [1–6]. Intensive research conducted so far indicated that the CDW and SC orders in TMDs compete unless they mutually exclude each other. In particular, studies found that T_{CDW} decreases, while T_c increases in the hexagonal (2H) polymorphs of TMDs from 2H-TaSe₂ through 2H-TaS₂ and 2H-NbSe₂ to 2H-NbS₂. In addition, it has been found that in 2H-NbSe₂, 2H-TaS₂, and 2H-TaSe₂, T_{CDW} decreases while T_c increases under pressure. On the other hand, the trigonal 1T-NbSe₂, 1T-TaS₂, and monoclinically distorted 1T'-TaTe₂ polymorphs show stable CDW phases at low temperature and no SC. In both 1T-TaS₂ and 1T'-TaTe₂, however, high pressure modifies the crystal lattice and SC emerges [7–13]. Studies on structurally distorted 2H-NbSe₂ concluded that CDWs may assist SC to a certain extent [14]. Altogether, these studies also indicated that changes in the lattice structure and/or its perfectness affect the competing CDW and SC orders differently, offering an opportunity to investigate the latter through carefully tuning the former. This opportunity has been explored in a number of studies on ternary TMDs, where one of the chalcogenide species has been systematically replaced by another with a goal to modify the

lattice structure such that the CDW order is suppressed and SC order induced. The studies took advantage of the fact that some TMD polymorphs and polytypes coexist at certain compositions and temperature [15–19], allowing us to make solid solution of different parent phases and study concurrent variations of the CDW and SC orders as the underlying lattice structure evolves. In particular, studies on 1T-TaSe_{2-x}S_x and 1T-TaSe_{2-x}Te_x systems indicated that the CDW state is suppressed and SC emerges in the middle of the phase diagram [20–22]. The effect was explained in term of chemical ordering effects and buckling of Ta planes, respectively. Studies on rhombohedral 3R-TaSe_{2-x}Te_x solid solutions attributed the observed increase in T_c in comparison to 2H-TaSe₂ to the difference in the stacking sequence of the TMD layers [23]. Studies on 2H-TaSe_{2-x}S_x solid solutions [24] reported the emergence of a strong SC order with S doping and broadly explained it in terms of increased structural disorder. In all these studies, the lattice structure features presumed to be behind the emergence and rise of a SC order have not been clearly revealed but inferred from weak changes in the contrast of scanning tunneling microscopy images, broadening of Bragg diffraction peaks and/or smearing of CDW related superstructure reflections. The reason for the observed asymmetry of $T_c(x)$ with the variation of x has not been revealed either. It is important to understand the factors that influence the CDW and SC orders in TMDs, in particular T_c , because room temperature superconductors of future technologies will most likely be assembled from pre-selected lattice structures with a particular chemistry taking advantage of basic

*petko1vg@cmich.edu

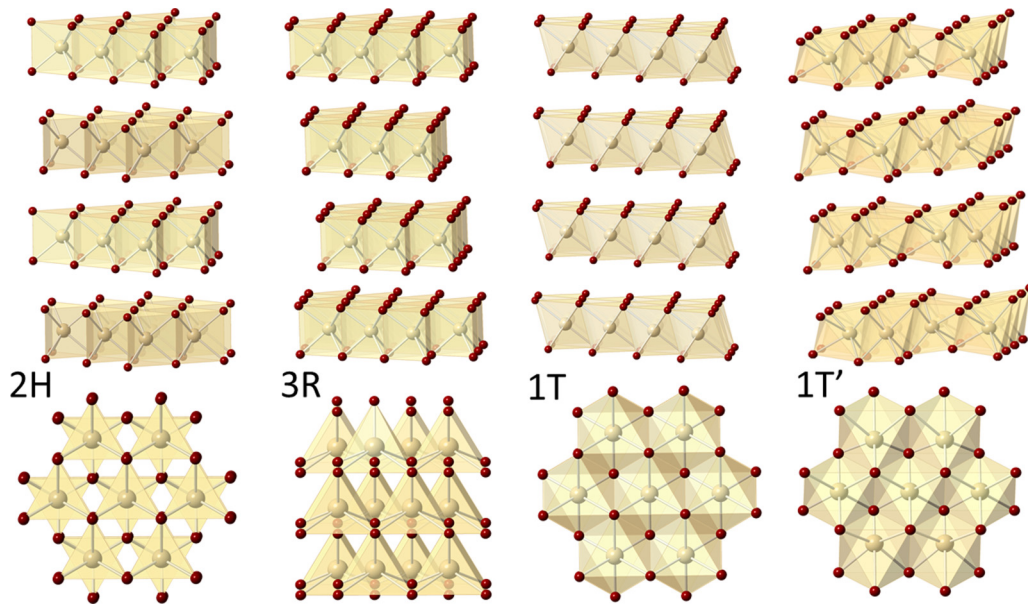


FIG. 1. Fragments of the $2H$ (hexagonal), $3R$ (rhombohedral), $1T$ (trigonal), and $1T'$ (monoclinic) TMD phases. Side view is shown in the first row and top view is shown in the second row. Both $2H$ and $3R$ phases are built of layers of regular trigonal prisms. The difference is in the stacking sequence of the layers. It is $ABAB$ and $ABCABC$ type with the $2H$ and $3R$ phase, respectively. Both $1T$ and $1T'$ phases are built of layers of octahedra. The difference is in the perfectness of the octahedra. They are regular and distorted in the $1T$ and $1T'$ phase, respectively. TM atoms are in light brown and chalcogenide atoms are in red.

mechanisms that lead to the enhancement of their useful properties.

Here we shed light on the influence of the lattice structure and perfection on the CDW and SC orders in TMDs by studying an exemplary Ta-based ternary TMD system using advanced x-ray scattering techniques and large-scale atomistic modeling [25,26]. We find that strong lattice distortions, such as buckling of Ta planes, are indeed detrimental to both the CDW and SC orders. Furthermore, we find that while perfect lattice order in two dimensions (2D) is enough for the CDW order to emerge, three-dimensional (3D) periodicity of Ta sublattice is necessary to achieve a SC ordered state. This could occur for markedly different degrees of substitution of the two chalcogenide species for one another and type of Ta coordination polyhedra, leading to a highly irregular evolution of $T_c(x)$ with x . Thus, a hierarchical relationship appears to exist among the crystal lattice, CDW, and SC orders in TMDs. We chose to study this relationship in Ta-Te-Se solid solutions extending between the stable polymorphs of their end members, that is $2H$ -TaSe₂ and $1T'$ -TaTe₂, where the crystal lattice, CDW, and SC orders have been observed to vary strongly [23]. The variation is to be expected because not only the type of crystal lattice in the end members but also the size and electronegativity of constituent Se and Te atoms are significantly different. This renders ternary the ($2H$ -TaSe₂)-($1T'$ -TaTe₂) system, hereafter referred to as TaSe_{2-x}Te_x, very suitable for the purposes of our study. Moreover, the isoelectronic substitution of Te for Se in the studied solid solutions allows us to concentrate largely on the effect of the lattice structure and perfectness on the CDW and SC orders in TMDs.

In particular, at atomic level, the end member $2H$ -TaSe₂ may be looked at as a stack of Ta-Se layers held together

by weak van der Waals interactions (Fig. 1). In a layer, one Ta atomic plane is sandwiched between two Se atomic planes, forming strong ionic bonds within a local trigonal prismatic unit. In the high-temperature normal state, hexagonal $2H$ -TaSe₂ is a bad metal with a pseudogap and c -axis resistivity 20–50 times larger than the in-plane resistivity. It undergoes a transition to an incommensurate (I)CDW phase at $T_{(I)CDW} \sim 122$ K with a modulation close to a $3a \times 3a$ superstructure, where a is the plane lattice parameter. Upon further cooling, $2H$ -TaSe₂ undergoes another transition into a commensurate (C) $3a \times 3a$ CDW phase at $T_{(C)CDW} \sim 90$ K, before finally becoming a superconductor at very low temperature ($T_c \sim 0.14$ K). In the CDW phase, Ta atoms appear displaced from their position in the underlying hexagonal lattice forming a 2D repetitive pattern of small, hexagonlike clusters [27–32].

The end member $1T'$ -TaTe₂ is also a bad metal. At atomic level, it may be looked at as a stack of Ta-Te layers where each layer is formed by a Ta atomic plane sandwiched between Te atomic planes, forming strong ionic bonds within a local octahedral unit (Fig. 1). In contrast to the uncommon trigonal $1T$ -TaSe₂ polymorph (Fig. 1), where Ta-Se octahedra are perfect, Ta-Te octahedra in $1T'$ -TaTe₂ are distorted, leading to an overall monoclinic distortion of the crystal lattice. It is considered that the distortion is due to the lower electronegativity of Te in comparison to Se, resulting in a relative weakening of Ta–Te bonds and partial charge transfer from Te to Ta. The structure is stabilized by metal-type Ta-Ta interactions, leading to the emergence of a CDW phase characterized by a $3a \times 1a$ superstructure featuring zigzag chains of Ta atoms. Upon cooling, $1T'$ -TaTe₂ undergoes a structural phase transition at about 170 K, where the double-zigzag chains of Ta atoms break down to strings of “butterfly”-like clusters.

No SC has been observed down to 0.05 K [33–38]. Little is known about the lattice structure of $\text{TaSe}_{2-x}\text{Te}_x$ solid solutions though.

II. EXPERIMENT

A. Sample preparation

Polycrystalline $\text{TaSe}_{2-x}\text{Te}_x$ solid solutions, where $x = 0, 0.2, 0.66, 1, 1.66, \text{ and } 2$, were made by conventional solid-state synthesis. In particular, high-purity powders of Ta (Alfa Aesar, 99.97%), Te (Alfa Aesar, 99.99%), and Se (Alfa Aesar, 99.999%) were mixed in appropriate stoichiometric ratios and thoroughly ground, pelletized, and heated in sealed evacuated silica tubes at 700 °C for 24 h. Subsequently, the as-prepared powders were reground, repelletized, and sintered again at 1000 °C for 48 h. The compositions reflect sections of the T_{CDW} and T_c vs composition x -phase diagram where the CDW and SC orders have been found to evolve markedly in different directions [23].

B. Synchrotron x-ray-diffraction (XRD) experiments and Rietveld analysis of the XRD patterns

The polycrystalline powders were subjected to XRD experiments using synchrotron x rays with energy of 105.7 keV ($\lambda = 0.1173 \text{ \AA}$). Data were collected at several temperatures ranging from 400 to 100 K at the beamline 11-ID-C at the Advanced Photon Source at the Argonne National Laboratory. The instrument was calibrated using Si powder (NIST) standard. Samples were sealed in glass capillaries and measured in transmission geometry. An empty glass capillary was measured separately. Scattered intensities were collected with a 2D amorphous Si detector. Oxford Cryostream 700+ device was used to control the temperature of the samples. Two sets of XRD patterns were collected at each temperature. One of the patterns was collected with the detector positioned 1000 mm away from the sample to achieve high- q resolution, where the wave vector q is defined as $q = 4\pi \sin(\theta)/\lambda$ and θ is the Bragg angle. This pattern was used to perform Rietveld analysis using the software GSAS II [39]. Experimental XRD patterns for $\text{TaSe}_{2-x}\text{Te}_x$ solid solutions and results from the analysis are summarized in Fig. 2. As can be seen in the figure, Rietveld fits confirm the average hexagonal and monoclinic structure of the end members $2H$ - TaSe_2 and $1T'$ - TaTe_2 , respectively. The Se-rich $\text{TaSe}_{1.8}\text{Te}_{0.2}$ solid solution was found to exhibit the structure of the uncommon rhombohedral $3R$ polymorph of TaSe_2 (shown in Fig. 1) whereas the XRD pattern for $\text{TaSe}_{1.66}\text{Te}_{0.34}$ could be barely reproduced by a structure model featuring a mixture of hexagonal $2H$ and monoclinic $1T'$ phases. The average crystal structure of TaSe_1Te_1 appeared to be of the trigonal $1T$ type shown in Fig. 1. The Te-rich solid solution $\text{TaSe}_{0.34}\text{Te}_{1.66}$ showed features consistent with the monoclinic-type structure of $1T'$ - TaTe_2 . As discussed below, the not quite conclusive Rietveld analysis of the XRD patterns for the solid solutions, except for $3R$ - $\text{TaSe}_{1.8}\text{Te}_{0.2}$, are largely due to the fact that they exhibit distinct Ta–Se and Ta–Te bonding distances, which are difficult to account for using lattice structure models constrained to traditional crystallography.

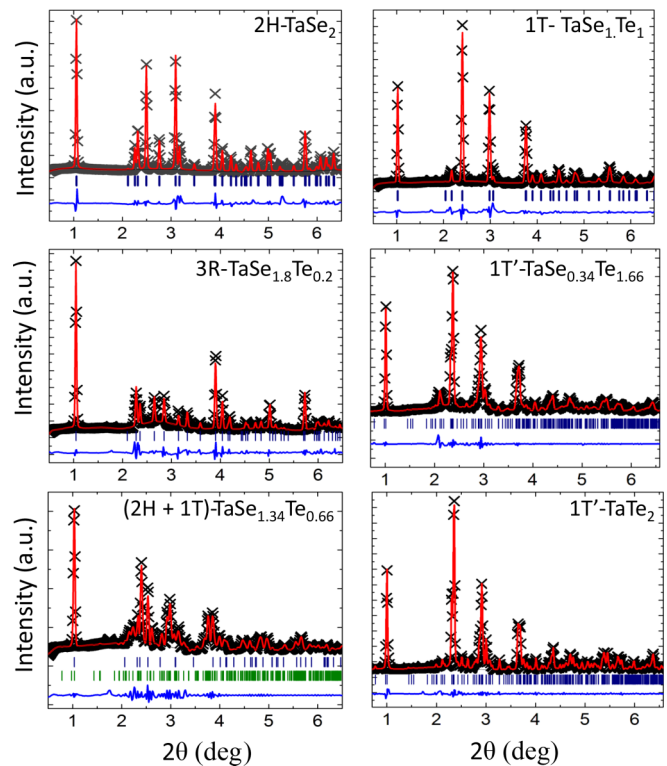


FIG. 2. Rietveld fit (red line) to high-energy XRD patterns (symbols) for $\text{TaSe}_{2-x}\text{Te}_x$ solid solutions collected at room temperature. In particular, the XRD patterns for TaSe_2 and $\text{TaSe}_{1.8}\text{Te}_{0.2}$ can be reasonably well fit with structure models based on the $2H$ and $3R$ phases shown in Fig. 1, respectively. The XRD pattern for $\text{TaSe}_{1.66}\text{Te}_{0.34}$ can be reproduced by a model featuring a majority $2H$ (blue bars) and a minority $1T$ (green bars) phases. The diffraction pattern for TaSe_1Te_1 can be reasonably well fit with a structure model based on the $1T$ phase shown in Fig. 1. Those for $\text{TaSe}_{0.34}\text{Te}_{1.66}$ and TaTe_2 can be reasonably well fit with a structure model based on the $1T'$ phase shown in Fig. 1. The residual difference between the experimental and computed XRD patterns (blue line) is shifted by a constant factor for clarity. Vertical bars designate Bragg peaks in the XRD patterns of the respective solid solutions.

C. Atomic pair-distribution analysis of synchrotron XRD data

The other pattern was collected with the detector positioned 300 mm away from the sample to reach q values as high as 30 \AA^{-1} . This pattern was used to obtain atomic pair-distribution functions (PDFs) with high real-space resolution as follows: At first, the separately measured signal arising from the glass capillary and sample environment, including air scattering, was subtracted from the respective pattern. Then, corrections for absorption in the sample and inelastic (Compton scattering) were applied following long-established procedures using an improved version of the software RAD [40]. The resulting data were scaled into absolute units and converted to the so-called reduced structure factor $q[S(q)-1]$. Finally, using a Fourier transform, the reduced structure factor was converted to a total atomic PDF. Total PDFs for $\text{TaSe}_{2-x}\text{Te}_x$ ($0 \leq x \leq 2$) solid solutions obtained at different temperature are summarized in Fig. 3. As defined, atomic PDFs peak at distances separating frequently occurring pairs of atoms, and the area under the peaks are proportional to

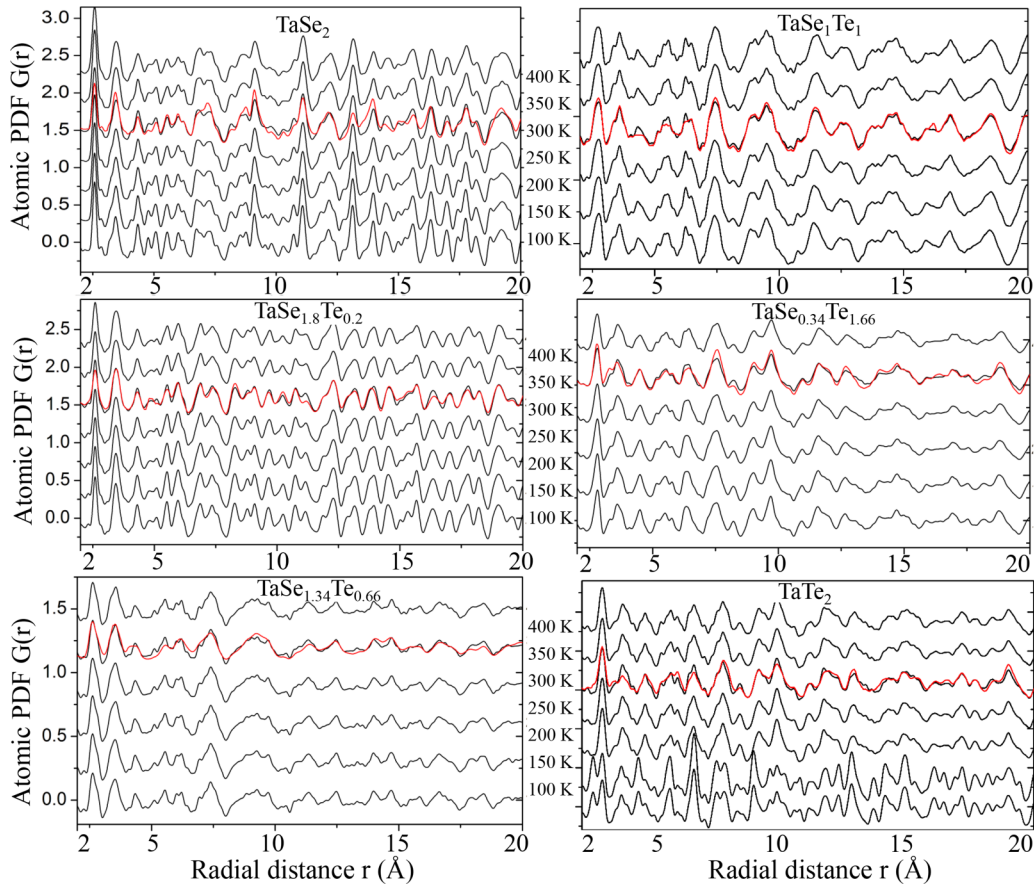


FIG. 3. Experimental total atomic PDFs for $\text{TaSe}_x\text{Te}_{2-x}$ solid solutions obtained at different temperature (black line). Experimental Ta-differential atomic PDFs obtained at room temperature (red line) are also shown.

the relative number of those pairs. This renders atomic PDFs very sensitive to details of crystal lattices in TMDs, including crystal lattice distortions [25,26,32].

To increase further the sensitivity of atomic PDFs for lattice features involving Ta atoms, we carried out resonant XRD experiments at the K edge of Ta. The experiments were carried out at the beamline 1-ID-C at the Advanced Photon Source at the Argonne National Laboratory at room temperature. The instrument was calibrated using Si powder (NIST) standard. The sample was measured twice, one time using x rays with energy of 67.406 keV ($\lambda = 0.1839$ Å) and a second time using x rays with energy of 67.106 keV ($\lambda = 0.1847$ Å).

The first energy is 10 eV and the second energy is 310 eV below the K -absorption edge of Ta (67.416 eV). Scattered intensities were collected to wave vectors of 28 Å $^{-1}$ using an energy-sensitive liquid N_2 -cooled Ge detector coupled to a multichannel analyzer. The analyzer allowed us to discriminate between the scattered x rays intensities in terms of their energy. By setting “energy windows” incorporating several neighboring channels of the analyzer, only elastic/coherent intensities scattered from the samples were obtained. Separately measured XRD data from an empty glass capillary were subtracted from the intensities, which were subsequently corrected for absorption in the sample using long-established procedures [40]. The higher-energy XRD pattern (10 eV below the K edge of Ta) was subtracted from the lower-energy XRD pattern (310 eV below the edge), and the difference was

Fourier transformed into the so-called Ta-differential atomic PDF. Since the intensity difference between the patterns is largely due to the difference in the x-ray scattering factor of Ta atoms at the two energies, Ta-differential PDFs reflect only atomic correlations involving Ta atoms, that is, Ta-Ta and Ta-chalcogenide atomic correlations. The resulting Ta-differential PDFs are shown in Fig. 3. For reference, the contribution of Ta-Ta atomic pairs to Ta-differential PDFs is about 50%. It is only 30 % in the case of total PDFs. More details of resonant high-energy XRD experiments and derivation of differential atomic PDFs can be found in Refs. [41,42].

Inspection of the PDFs in Fig. 3 indicates that the crystal lattices in the solid solutions with $x > 0.2$ appear more distorted in comparison to $2H$ - TaSe_2 and $3R$ - $\text{TaSe}_{1.8}\text{Te}_{0.2}$. This is because peaks in the PDFs for the former are less sharp in comparison to corresponding peaks in the PDFs for the latter. To investigate the reason, in Fig. 4(a) we compared the low- r part of the experimental total PDFs obtained at room temperature. As can be seen in the figure, the first PDF peak, i.e., the first coordination sphere in $2H$ - TaSe_2 and $3R$ - $\text{TaSe}_{1.8}\text{Te}_{0.2}$ is well-defined and narrow, indicating the presence of a unique Ta-chalcogenide bond length. By contrast, the first peak in the PDFs for the other compositions appear either rather broad, as is the case with the end member $17'$ - TaTe_2 and $\text{TaSe}_{0.34}\text{Te}_{1.66}$, or split into two components, as is the case with $\text{TaSe}_{1.34}\text{Te}_{0.66}$, and TaSe_1Te_1 solid solutions, indicating the presences of different Ta-chalcogenide bond lengths. The

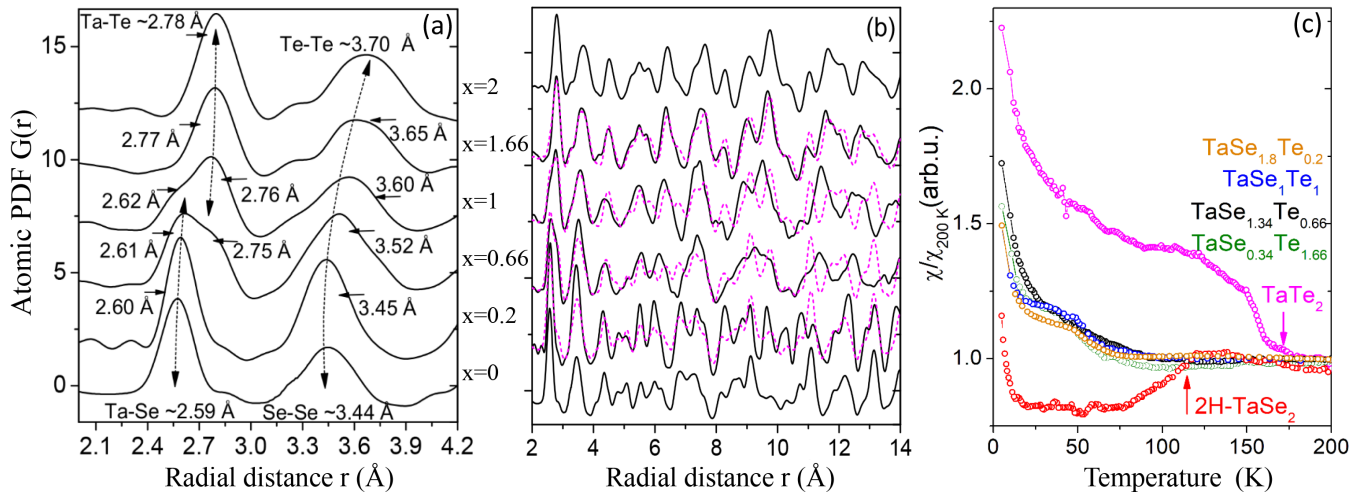


FIG. 4. (a) Evolution of the first two peaks in the experimental total PDFs for $\text{TaSe}_{2-x}\text{Te}_x$ solid solutions with Te content, x . The first peak reflects Ta–chalcogenide bonding distances and appears split into two components for the solid solutions with $x = 0.66$ and $x = 1$, indicating the presence of short Ta–Se and long Ta–Te bonding distances. The distances change little with x (see arrows). The second PDF peak largely reflects chalcogenide–chalcogenide bonding distances that are seen to increase gradually with x . (b) Experimental (black line) and model (broken magenta line) total PDFs for $\text{TaSe}_{2-x}\text{Te}_x$ solid solutions obtained at room temperature. The model PDFs are a properly weighted average of the experimental PDFs for the end members TaSe_2 and TaTe_2 . The model and experimental PDFs disagree, indicating that the solid solutions are single phase and not mixtures of segregated TaSe_2 and TaTe_2 phases. (c) Magnetic susceptibility for $\text{TaSe}_{2-x}\text{Te}_x$ solid solutions. Data are normalized against the respective values measured at 200 K. The magnetic susceptibility for the end members TaSe_2 and TaTe_2 exhibits a well-defined transition at about 120 and 170 K, respectively (see arrows), reflecting the onset of CDW order. No such transition is observed with the solid solutions.

evolution of the first peak in the PDFs for $\text{TaSe}_{2-x}\text{Te}_x$ solid solutions indeed resembles very much that of the first peak in the PDFs for single-phase $\text{In}_x\text{Ga}_{1-x}\text{As}$ solid solutions exhibiting distinct In–As and Ga–As bonding distances [43]. Here the presence of different Ta–Te bonding distances in $1T'$ - TaTe_2 reflects the strong periodic lattice distortions characteristic to its room-temperature CDW phase [33]. The presence of two types of bonding distances in Ta–Te–Se solid solutions has been assumed but never clearly proven by experiment as done here. Atomic PDFs computed as a properly weighted average of the experimental PDFs for the end members are compared with the experimental PDFs for the solid solutions in Fig. 4(b). The comparison shows that the solutions are not mixtures of segregated $2H$ - TaSe_2 and $1T'$ - TaTe_2 phases but assemblies of interfused Ta–chalcogenide coordination polyhedra exhibiting bonding distances that evolve with the relative Se to Te ratio.

D. Magnetic measurements

Experimental data for the magnetic susceptibility of $\text{TaSe}_{2-x}\text{Te}_x$ solid solutions are shown in Fig. 4(c). Data were obtained on a standard physical property measuring system instrument from Quantum Design using the vibrating sample magnetometer mode of operation. They confirm the well-known changes in the atomic and electronic structure of the end members taking place at about 120 and 170 K, respectively, where they undergo a phase transition to CDW phases persisting to very low temperature, thus preventing the emergence of SC [11,23,33,37]. Data for the solid solutions do not show such transitions down to 5 K, indicating that their room-temperature atomic structure persists to very low temperature.

The smooth evolution of the respective atomic PDFs in Fig. 3 with decreasing temperature indicates the same.

III. 3D LATTICE STRUCTURE MODELING

Due to the presence of lattice distortions and a variety of Ta–chalcogenide coordination spheres, a description of $\text{TaSe}_{2-x}\text{Te}_x$ solid solutions in terms of some average crystallographic unit cell may not be necessarily accurate enough to capture their specific lattice structure in good detail [22,23]. Therefore, we constructed large-scale atomistic models for $\text{TaSe}_{2-x}\text{Te}_x$ solid solutions and refined them against the respective total and Ta–differential PDFs using reverse Monte Carlo computations [44]. The advantage of such modeling over crystallography-constrained Rietveld/PDF analysis is the ability to test and refine lattice structures involving distinct chalcogenide species that are known to induce different coordination environments, e.g., trigonal prismatic for Se and octahedral-like for Te, and also exhibit different TM–chalcogenide bonding distances. Large-scale 3D structure models for $\text{TaSe}_{2-x}\text{Te}_x$ solid solutions were based on approximately $100 \text{ \AA} \times 100 \text{ \AA} \times 100 \text{ \AA}$ configurations comprising from 80 000 to 90 000 Ta, Se, and Te atoms in due proportions. The initial configurations represented cuts from the crystal lattices found plausible by Rietveld analysis of the respective XRD patterns. For each composition, the initial configuration was refined against the total and Ta–differential data sets obtained at 300 K and a model for the room temperature lattice structure was produced. The model was used as an initial guess for the lattice structure at 250 K and refined further against the respective PDF data. Following the same approach, we built a sequence of models

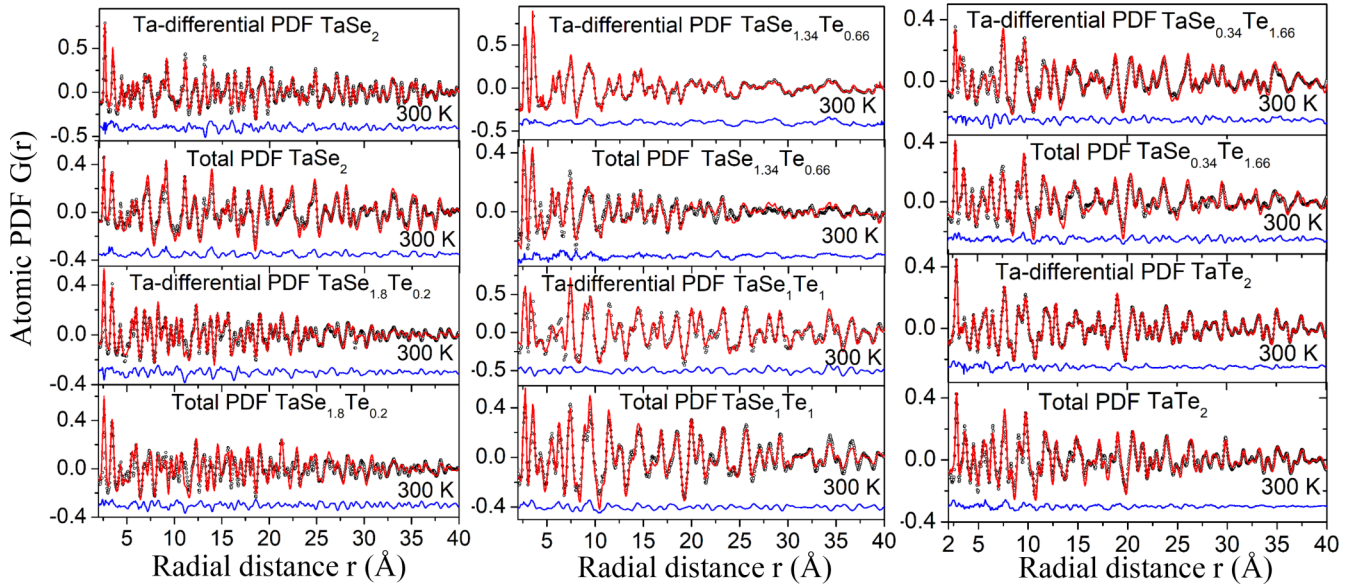


FIG. 5. RMC fits (red line) to experimental total and Ta-differential atomic PDFs (symbols) for $\text{TaSe}_{2-x}\text{Te}_x$ solid solutions obtained at room temperature. The residual difference (blue line) is shifted by a constant factor for clarity. The goodness-of-fit indicator for the fits is about 10%.

tracking the evolution of the lattice structure and distortions in $\text{TaSe}_{2-x}\text{Te}_x$ solid solutions upon cooling from room temperature down to 100 K. Note that this temperature range includes T_{CDW} for the end members $2H$ - TaSe_2 and $1T'$ - TaTe_2 . During the refinement, restraints for bonding distances and coordination numbers in the model configurations were imposed. In particular, Ta, Se, and Te atoms were restrained not to approach each other closer than the sum of the respective ionic radii. Also, Ta-chalcogenide and chalcogenide-Ta first coordination numbers were restrained to stay close to 6 and 3, respectively, thus accounting for the specifics of the crystal structure types exhibited by TMDs. The refinements were done using a new version of the computer program RMC++ [45]. Exemplary RMC fits to atomic PDFs obtained at room temperature are shown in Fig. 5. Exemplary RMC fits to atomic PDFs obtained at 100 K are shown in Fig. S1 in the Supplemental Material (SM) [46]. As can be seen in the figures, the RMC models obtained here reproduce the experimental PDF data in very good detail. Fragments of the RMC refined model structures for $\text{TaSe}_{2-x}\text{Te}_x$ solid solutions at 100 K are shown in Fig. 6. Results of analysis of the models in terms of chalcogenide-Ta-chalcogenide and Ta-Ta-Ta bond angles are shown in Fig. 7. The angles provide information for the type and distortion of Ta-chalcogenide polyhedral units. Also shown in Fig. 7 are Ta-Ta-Ta-Ta dihedral angles in Ta planes. These angles provide information for deviations of Ta atoms from their expected positions in the undistorted hexagonal TM layers found in $2H$, $3R$, and $1T$ polymorphs of TMDs, in particular buckling of the layers [47]. Partial Ta-Ta and chalcogenide-chalcogenide PDFs computed from the models are shown in Fig. 8(a) and Fig. S2 in the SM, respectively. The functions describe, respectively, the arrangement of atoms in Ta and chalcogenide (Se and/or Te) sublattices in $\text{TaSe}_{2-x}\text{Te}_x$ solid solutions. These lattice structural characteristics are known to affect strongly the CDW and SC orders in TMDs [1,11].

IV. DISCUSSION

The stacking sequence of chalcogenide and TM atomic planes in TM-chalcogenide layers and the type of resulting TM-chalcogenide coordination polyhedra have a profound effect on the electronic properties of TMDs, including the emergence of CDW and SC orders [15,48]. Two factors have been found to determine the type of chalcogenide polyhedra about TM atoms in TMDs to a large extent. Those are the ionicity of TM-chalcogenide bond and relative size (radii) of TM and chalcogenide ions. The ionicity, i.e., distribution of charge, in TMDs is largely determined by the electronegativity of the constituent atoms. The radii of TM and chalcogenide ions in TMDs also vary as a function of the electronegativity difference of the constituent atoms. The implication is that, because of their dependence on the system's chemistry, these radii cannot be assigned some assumed universal values but have to be evaluated carefully for the particular TMD system under consideration. This is particularly true for TMDs where the bonding is not entirely ionic in character. Gamble [49] has proposed an elegant method to evaluate the preference of TMDs for trigonal-prismatic vs octahedral coordination of TM atoms. It is based on the ratio, $R_{\text{TM}}^+/R_{\text{Ch}}^-$, of the actual radii of TM (R_{TM}^+) and chalcogenide (R_{Ch}^-) ions in the TMD system under consideration, as determined from experimental diffraction data. The critical radius ratio at which chalcogenide ions on opposite sides of a TMD layer (see Fig. 1) would come into contact is $R_{\text{TM}}^+/R_{\text{Ch}}^- = 0.527$ for an ideal trigonal-prismatic coordination. For TMDs based on Nb and Ta, the trigonal-prismatic structure is maintained until that ratio is larger than 0.49 [49,50]. The octahedral coordination would be adopted when the $R_{\text{TM}}^+/R_{\text{Ch}}^-$ ratio is below 0.49, thereby permitting a closer approach of large chalcogenide ions to the TM cations and hence the attainment of R_{TM}^+ to R_{Ch}^- bond length dictated by the system's chemistry and electronegativity difference. Note that when the trigonal prismatic voids are filled with TM atoms the planes of TM and chalcogenide atoms forming

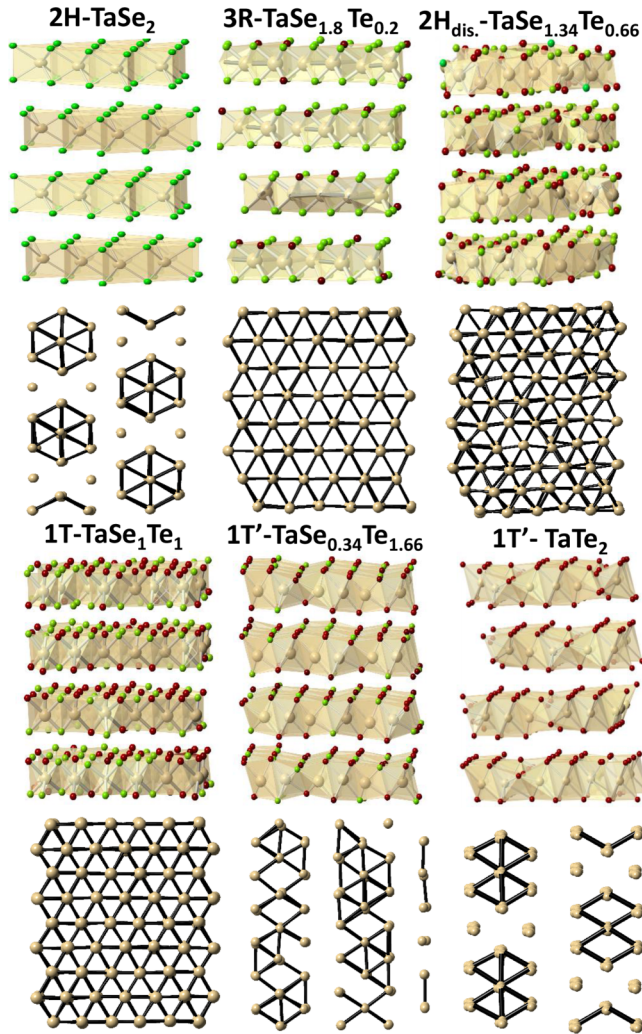


FIG. 6. Fragments representing side view of the layers of polyhedra in $\text{TaSe}_{2-x}\text{Te}_x$ solid solutions at 100 K as obtained by RMC modeling guided by experimental atomic PDFs. The structure type of each model, $2H$, $3R$, $1T$, or $1T'$, is given on top of the respective fragment. As the modeling results show, layers in $2H$ - TaSe_2 and $3R$ - $\text{TaSe}_{1.8}\text{Te}_{0.2}$ are made of well-defined trigonal prisms. Layers in $2H_{\text{dis}}$ - $\text{TaSe}_{1.34}\text{Te}_{0.66}$ are made of heavily distorted trigonal prisms. Layers in $1T$ - TaSe_1Te_1 are made of well-defined octahedra. Layers in $1T'$ - $\text{TaSe}_{0.34}\text{Te}_{1.66}$ and $1T'$ - TaTe_2 are made of distorted octahedra (distorted trigonal antiprisms). Top view of an individual Ta atomic plane in $\text{TaSe}_{2-x}\text{Te}_x$ solid solutions is given beneath the respective fragment. The plane is obtained by mapping out all Ta planes in the respective 3D model onto a single Ta plane. Thick black lines connect Ta atoms to highlight their local arrangement. In particular, Ta atoms in the end members $2H$ - TaSe_2 and $1T'$ - TaTe_2 are clustered in hexagons and strings of butterflylike clusters, respectively. Local clustering of Ta atoms in double chains is also seen in the model for $1T'$ - $\text{TaSe}_{0.34}\text{Te}_{1.66}$. On the other hand, Ta atoms in the models for $3R$ - $\text{TaSe}_{1.8}\text{Te}_{0.2}$ and $1T$ - TaSe_1Te_1 make near-perfect hexagonal planes. Notably, the Ta layer in the model for $\text{TaSe}_{1.34}\text{Te}_{0.66}$ appears heavily distorted. Ta atoms are in light brown, Se atoms are in green, and Te atoms are in red.

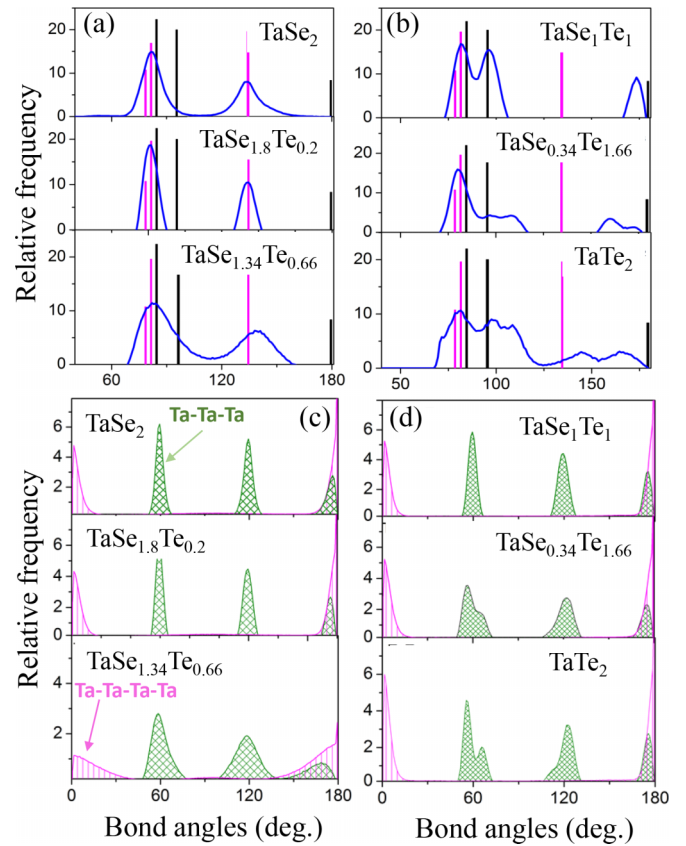


FIG. 7. (a), (b) Chalcogenide–Ta–chalcogenide bond angles for $\text{TaSe}_{2-x}\text{Te}_x$ solid solutions at 100 K (blue line), as extracted from the respective RMC refined models. Chalcogenide–Ta–chalcogenide bond angles for undistorted trigonal prismatic (magenta bars) and octahedral (black bars) coordination found with the $2H$ and $1T$ TMD phases, respectively, are also shown. (c), (d) Ta–Ta–Ta bonding (green) and Ta–Ta–Ta–Ta dihedral (magenta) angles for $\text{TaSe}_{2-x}\text{Te}_x$ solid solutions at 100 K. The end member $2H$ - TaSe_2 and the solid solutions poor in Te (left-hand side of the plot) exhibit trigonal-prismatic Ta coordination. The trigonal prisms are regular in $2H$ - TaSe_2 and $\text{TaSe}_{1.8}\text{Te}_{0.2}$, as indicated by the narrower distribution of chalcogenide–Ta–chalcogenide bond angles in (a). The prisms in $\text{TaSe}_{1.34}\text{Te}_{0.66}$ appear very distorted, as indicated by the very broad distribution of chalcogenide–Ta–chalcogenide bond angles in (a). The end member $1T'$ - TaTe_2 and the solid solution rich in Te (right-hand side of the plot) exhibit octahedral Ta coordination. The octahedra in TaSe_1Te_1 are fairly regular, as indicated by the narrow distribution of chalcogenide–Ta–chalcogenide bond angles in (b). The octahedra in $\text{TaSe}_{0.34}\text{Te}_{1.66}$ and $1T'$ - TaTe_2 are quite distorted, as indicated by the nonuniformity of chalcogenide–Ta–chalcogenide bond angle distribution in (b). Ta–Ta–Ta bond angles in $2H$ - TaSe_2 (c), $\text{TaSe}_{1.8}\text{Te}_{0.2}$ (c), and TaSe_1Te_1 (d) are narrow, reflecting the 2D pattern of Ta hexagons in these solid solutions. The distribution of Ta–Ta–Ta bond angles in $\text{TaSe}_{1.34}\text{Te}_{0.66}$ (c), $\text{TaSe}_{0.34}\text{Te}_{1.66}$ (d), and $1T'$ - TaTe_2 (d) is not uniform, reflecting the distortions of Ta hexagons in these solid solutions. The distribution of Ta–Ta–Ta–Ta dihedral angles in $\text{TaSe}_{1.34}\text{Te}_{0.66}$ (c) is very smeared, reflecting the buckling of Ta planes. These planes appear fairly flat in the other solid solutions, as indicated by the uniformity of the respective Ta–Ta–Ta–Ta bond angle distributions (c) and (d).

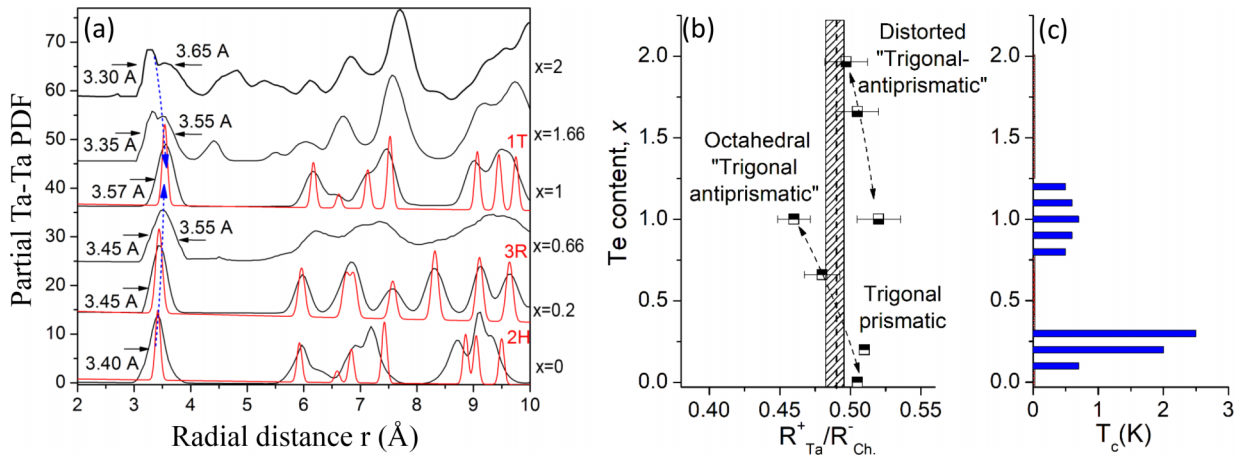


FIG. 8. (a) Partial Ta-Ta PDFs for $\text{TaSe}_{2-x}\text{Te}_x$ solid solutions computed (black line) from refined RMC models and ideal crystal lattices (red line) discussed in the text. The first peak reflects first neighbor Ta-Ta distances. It appears split for $1T'$ - TaTe_2 and $1T'$ - $\text{TaSe}_{0.34}\text{Te}_{1.66}$ (see the arrows) reflecting the local clustering of Ta atoms, as shown in Fig. 6. The first peak in the PDF for $\text{TaSe}_{1.34}\text{Te}_{0.66}$ is rather broad, reflecting the presence of strong distortions in Ta planes, as shown in Fig. 6. The first peak in the PDF for $2H$ - TaSe_2 is asymmetric, reflecting the presence of hexagonlike clusters, as shown in Fig. 6. The first peak in the PDFs for $3R$ - $\text{TaSe}_{1.8}\text{Te}_{0.2}$ and $1T$ - TaSe_1Te_1 is well defined, reflecting the absence of Ta clustering, as shown in Fig. 6. Blue arrows emphasize the evolution of average Ta-Ta bonding distances in $\text{TaSe}_{2-x}\text{Te}_x$ solid solutions with the relative Te content. Note that interlayer Ta-Ta distances alone extend to about 7 Å. Distances at higher- r values reflect both Ta-Ta intra- and interlayer correlations. Only for $3R$ - $\text{TaSe}_{1.8}\text{Te}_{0.2}$ ($x = 0.2$) and $1T$ - TaSe_1Te_1 ($x = 1$) solid solutions Ta-Ta PDFs are lined up with the Ta-Ta PDFs for the respective undistorted lattices at higher- r distances, indicating that Ta sublattices in these solid solutions are periodic in 3D. This is not the case with the end members and other solid solutions. (b) Ratio of the average radius of Ta cation, R_{Ta}^+ and chalcogenide ion, R_{Ch}^- for $\text{TaSe}_{2-x}\text{Te}_x$ solid solutions (symbols). The radii are determined from the position of the first peak in the total and chalcogenide-chalcogenide PDFs, respectively, as explained in the SM. Horizontal bars reflect variations in that ratio arising from the presence of distinct Ta-chalcogenide and chalcogenide-chalcogenide bonding distances in the respective solid solutions, as explained in the SM. Hatched rectangle highlights the critical ratio R_{Ta}^+/R_{Ch}^- of 0.49 corresponding to the stability limit of TMDs with octahedral (<0.49) and trigonal-prismatic (>0.49) Ta coordination [47–50]. Broken lines emphasize the increasing instability of the trigonal-prismatic and distorted octahedral coordination of Ta atoms in $\text{TaSe}_{2-x}\text{Te}_x$ solid solutions with the increase and decrease of Te content, respectively. Likely due to the instability, the coordination polyhedra in $1T$ - TaSe_1Te_1 appear as near-regular octahedra. Note that undistorted and distorted octahedra in Te-rich solid solutions may be viewed as undistorted and distorted trigonal antiprisms, respectively. Overall, Te-poor and Te-rich solid solutions appear on two different branches of the evolution of R_{Ta}^+/R_{Ch}^- ratios with Te percentage, each reflecting a particular coordination environment. The presence of such branches may be expected because of the different electronegativity of Se and Te [47–50]. (c) Observed T_c for $\text{TaSe}_{2-x}\text{Te}_x$ solid solutions (blue bars) [1, 11, 21–23]. The correlation between the data sets in (a), (b), and (c) is discussed in the text.

TM layers are not close packed, while close packing does result from the filling of octahedral voids. Values of the radius ratio R_{Ta}^+/R_{Ch}^- for $\text{TaSe}_{2-x}\text{Te}_x$ solid solutions studied here, as evaluated from experimental Ta-chalcogenide [Fig. 4(a)] and chalcogenide-chalcogenide bonding distances (Fig. S2), are summarized in Fig. 8(b). More details for the derivation of radius ratios R_{Ta}^+/R_{Ch}^- can be found in the SM. Analysis of the RMC refined structure models for $\text{TaSe}_{2-x}\text{Te}_x$ solid solutions at 100 K shows that, below T_{CDW} , Ta atoms in the CDW phase of $2H$ - TaSe_2 form a 2D superstructure of hexagon shaped 7-atom clusters (see Fig. 6). Also, Ta-Se trigonal prisms in $2H$ - TaSe_2 appear somewhat distorted because of the independent displacement of Ta and Se atoms along and perpendicular to Ta-Se layers, respectively, as indicated by the broadening of Se-Ta-Se bond angle distribution (Fig. 7). The layers of Ta atoms, however, remain fairly flat, as indicated by the narrow distribution of Ta-Ta-Ta-Ta dihedral angles around $0^\circ/180^\circ$. Overall, the Ta sublattice does not appear lined up with the average crystal lattice over long-range distances, i.e., the translational periodicity of Ta sublattice is broken in 3D, as documented by the disagreement between the positions of higher- r Ta coordination spheres computed from the respec-

tive RMC model and undistorted $2H$ lattice [Fig. 8(a)]. This 2D periodic lattice distortion and related charge localization (CDW) are rather stable and, as shown in many studies, a SC order barely emerges in $2H$ - TaSe_2 at extremely low temperature ($T_c = 0.14$ K) [1, 8, 11]. At a relatively low level of doping with Te, i.e., for $x = 0.2$, the trigonal-prismatic $3R$ polymorph of TaSe_2 appears more stable than the $2H$ polymorph, as indicated by the increased R_{Ta}^+/R_{Ch}^- ratio [Fig. 8(b)]. Because Te (ionic radius of about 1.85 Å; see Fig. S2) is larger than Se (ionic radius of about 1.72 Å; see Fig. S2), Ta-chalcogenide coordination polyhedra in $\text{TaSe}_{1.8}\text{Te}_{0.2}$ appear a bit expanded in comparison to those in $2H$ - TaSe_2 [compare Ta-chalcogenide bonding distances in Fig. 4(a)]. As a result, distances between Ta atoms in adjacent polyhedra also appear increased [compare Ta-Ta PDFs in Fig. 8(a)]. This quenches Ta-Ta interactions and the periodic 2D lattice distortions characteristic to the CDW ordered phase of the end member $2H$ - TaSe_2 disappear in $3R$ - $\text{TaSe}_{1.8}\text{Te}_{0.2}$ (Fig. 6).

In particular, Ta atoms in $\text{TaSe}_{1.8}\text{Te}_{0.2}$ are not clustered but appear arranged in a perfect hexagonal pattern (see the characteristic Ta-Ta-Ta bond angles of 60° , 120° , and 180° in Fig. 7) along noncorrugated Ta planes (see Ta-Ta-Ta-Ta

dihedral angle distribution in Fig. 7), ultimately forming a 3D lattice lined up with the average $3R$ -crystal lattice [see Ta-Ta partial PDF in Fig. 8(a)]. As a result of the restored translational periodicity, $3R$ $\text{TaSe}_{2-x}\text{Te}_x$ ($0.1 < x < 0.3$) solid solutions are found to exhibit a SC order where T_c increases with x [Fig. 8(c)] [11,23].

Further doping with Te, i.e., for $x = 0.66$, destabilizes the trigonal-prismatic coordination of Ta [Fig. 8(b)] because the increasing in number larger Te^{2-} ions could not come close enough to Ta^{4+} ions and attain the R_{Ta}^{4+} to R_{Te}^{2-} bond length dictated by the electronegative difference between Ta and Te atoms. This renders the crystal lattice of $\text{TaSe}_{1.34}\text{Te}_{0.66}$ solid solution heavily distorted (Fig. 6) at atomic level. In particular, Ta coordination polyhedra both appear distorted (see chalcogenide-Ta-chalcogenide bond angle distribution in Fig. 7) and exhibit two sets of bonding distances [Fig. 4(a)]. Because of reasons discussed above, on average, distances between nearby Ta atoms increase further in comparison to $\text{TaSe}_{1.8}\text{Te}_{0.2}$ [see Fig. 8(a)], indicating no Ta-Ta interactions. However, Ta planes appear heavily corrugated (see the broad distribution of Ta-Ta-Ta-Ta angles in Fig. 7) and Ta sublattice strongly deviates from the crystal lattices of known $2H$, $3R$, and $1T$ polymorphs of TMDs [see Ta-Ta PDFs in Fig. 8(a)], hardly exhibiting a periodic pattern. Not surprisingly, $\text{TaSe}_{2-x}\text{Te}_x$ solid solutions where $0.4 < x < 0.7$ do not show collective electronic states such as CDWs and SC [1,11,23].

When Se and Te atoms in $\text{TaSe}_{2-x}\text{Te}_x$ solid solutions are in near-equal percentages, the intrinsic for the end members trigonal prismatic ($2H$ - TaSe_2) and distorted octahedral/trigonal antiprismatic ($1T'$ - TaTe_2) coordinations of Ta atoms would be very unstable to coexist side by side [see the diverging ionic radius ratios in Fig. 8(b)]. As a result, the octahedral TM coordination is adopted instead to achieve a close-packed structure, thus minimizing atomic-level strain energy (see chalcogenide-Ta-chalcogenide bond angles in Fig. 7). Regardless of the presence of two sets of Ta-chalcogenide bonding distances [see Fig. 4(a)], Ta atoms appear arranged in a perfect hexagonal pattern (see Ta-Ta-Ta bond angles in Fig. 7) along flat Ta planes (see Ta-Ta-Ta-Ta dihedral angles distribution in Fig. 7). Also, for reasons discussed above, on average, Ta atoms appear pushed even further apart [see Ta-Ta PDFs in Fig. 8(a)] indicating no Ta-Ta interactions. Moreover, Ta atoms form a 3D periodic lattice lined up with the average $1T$ -type crystal lattice [Fig. 8(a)]. Not surprisingly, $\text{TaSe}_{2-x}\text{Te}_x$ solid solutions with $x = 1 \pm 0.3$ are found to exhibit a SC order [Fig. 8(c)] [8,21,23].

Because of the considerably distorted octahedral Ta coordination (see chalcogenide-Ta-chalcogenide bond angles in Fig. 7) nearby Ta atoms appear closer to each other in Te-rich $\text{TaSe}_{2-x}\text{Te}_x$ solid solutions, i.e., for $x = 1.66$, in comparison to TaSe_1Te_1 [see Fig. 8(a)], indicating increased Ta-Ta interactions and clustering (Fig. 6). Regardless of the distortion of Ta coordination polyhedra, Ta planes are flat, thus maintaining a considerable CDW order (see Ta-Ta-Ta-Ta angle distributions in Fig. 7). A similar picture is seen with the end member $1T'$ - TaTe_2 where Ta coordination polyhedra appear even further distorted, Ta atoms interact strongly, and form a 2D periodic pattern of butterflylike clusters (Fig. 6). The translational periodicity of Ta sublattice is broken in 3D [see

the respective Ta-Ta PDFs in Fig. 8(a)], precluding the emergence of SC order [21,23,33,34].

Positive external pressure is known to increase considerably T_c in both $2H$ - TaSe_2 and $1T'$ - TaTe_2 [10–13]. Positive external pressure would promote the emergence of a more close-packed lattice structure in $1T'$ - TaTe_2 by diminishing the distortions of building octahedral units, and therefore diminish Ta-Ta interactions, accompanied by an increase in Ta-Ta separations and 3D periodicity of Ta sublattice. This would promote the emergence of SC as the positive chemical pressure induced by substituting smaller Se atoms for larger Te atoms in Te-rich $\text{TaSe}_{2-x}\text{Te}_x$ solid solutions does. Increasing positive external pressure would also promote the emergence of a more close-packed lattice structure in $2H$ - TaSe_2 by increasingly modifying the trigonal-prismatic coordination of Ta atoms towards a more octahedral-like coordination. Effectively, this would at least frustrate Ta-Ta interactions, which are much weaker than Ta-Ta interactions in $1T'$ - TaTe_2 . In addition, it would increase some Ta-Ta separations at the expense of others and therefore increasingly restore the 3D periodicity of Ta sublattice, thus promoting the emergence of SC order. As the results of our study show, unless the $3R$ phase is directly stabilized, a similar effect takes place in Se-rich $2H$ - $\text{TaSe}_{2-x}\text{Te}_x$ solid solutions ($0.66 < x < 1$) when larger Te atoms are substituted for smaller Se atoms. This is because the resulting negative chemical pressure and related local lattice disorder are increasingly counteracted by the need to attain proper Ta-Te bonding distances and the resulting strong tendency of Ta and chalcogenide atomic planes to pack as close as possible in Ta-chalcogenide layers. For Se-rich $1T'$ - $\text{TaSe}_{2-x}\text{Te}_x$ solid solutions, the substitution of larger Te atoms for smaller Se atoms in the chalcogenide coordination octahedra of Ta atoms will simply increase the separation between Ta atoms centering adjacent octahedra, quench Ta-Ta interactions, and trigger the emergence of SC order at a given degree of substitution, as observed by experiment [21,23].

V. CONCLUSION

Results of our study show that the emergence of collective electronic states in TMDs, such as CDWs and SC, depends strongly on the type of underlying lattice structure and its perfectness. TMDs exhibiting strong lattice distortions, including buckling of TM planes, do not exhibit CDW and SC orders. TMDs exhibiting high lattice order in 2D can host electronic states periodic in 2D such as CDWs. 3D periodic order of the TM sublattice is necessary for the TMDs to exhibit a SC order. The SC order can appear both in TMDs with trigonal prismatic and in TMDs with octahedral coordination spheres comprising different chalcogenide species in different proportions. Evidently, at least in Ta-Se-Te solid solutions, the SC order does not depend critically on the degree of chalcogenide substitution. Indeed, a SC order has been observed in all Se ternary TMD solid solutions where the TM sublattice alone has been doped with other metal species, such as $\text{Ta}_{1-x}\text{TM}_x\text{Se}_2$ solid solutions (TM = Mo or W) [51].

Distortions of TM coordination polyhedra due to the presence of distinct TM-chalcogenide bonding distances, however, appear to degrade the SC order to a certain extent, as

a comparison between structure [Fig. 4(a)] and T_c [Fig. 8(c)] data for $3R\text{-TaSe}_{1.8}\text{Te}_{0.2}$ and $1T\text{-Se}_1\text{Te}_1$ indicates. This result does not necessarily contradict Anderson's theorem that T_c may not be suppressed by nonmagnetic impurities [52]. Merely, and in line with other studies [53–57], it indicates that in TMDs there are possibilities for electronic correlation and hence T_c degradation behavior due to local lattice distortions, in particular significant bond-length disorder, and minimization of such distortions may be important for raising T_c . The presence of local lattice distortions due to TM-chalcogenide bonding effects and different Ta coordination polyhedra that evolve irregularly with the chalcogenide substitution may also well explain the asymmetry of $T_c(x)$ vs x evolution observed with other ternary TMD solid solutions [20–24]. What appears to be of a critical importance to the SC order is the 3D periodicity of TM sublattice and separation between TM atoms, where an increased separation signals diminished TM-TM interactions and a potential for the emergence of SC order provided the 3D periodicity of TM sublattice also increases [compare data in Figs. 8(a) and 8(c)].

Lastly, results of the present study show that the crystal lattice in TMDs can simultaneously accommodate different coordination polyhedra and distortions that promote collective electronic states requiring different translational periodicity, e.g., 2D or 3D, to a different extent. These lattice imperfections can be modified and the states induced as desired, including one by one. Advanced x-ray scattering techniques can provide atomic-level feedback on such an effort, helping exploit fully the great potential of TMDs for practical applications.

ACKNOWLEDGMENTS

This work was supported by the U.S. Department of Energy, Office of Science, Office of Basic Energy Sciences under Award No. DE-SC0006877 and used resources of the Advanced Photon Source, a U.S. Department of Energy (DOE) Office of Science User Facility operated for the DOE Office of Science by Argonne National Laboratory under Contract No. DE-AC02-06CH11357. Thanks are due to O. Shovon and K. Chapagain for the help with the synchrotron XRD experiment.

-
- [1] K. Rossnagel, *J. Phys.: Condens. Matter* **23**, 213001 (2011).
- [2] H. Yang, S. W. Kim, M. Chhowalla, and Y. H. Lee, *Nat. Phys.* **13**, 931 (2017).
- [3] X. Zhu, J. Guo, J. Zhang, and E. W. Plummer, *Adv. Phys. X* **2**, 622 (2017).
- [4] C.-W. Chen, J. Choe, and E. Morrosan, *Rep. Prog. Phys.* **79**, 084505 (2016).
- [5] G. H. Han, D. L. Duong, D. H. Keum, S. J. Yun, and Y. H. Lee, *Chem. Rev.* **118**, 6297 (2018).
- [6] G. Gye, E. Oh, and H. W. Yeon, *Phys. Rev. Lett.* **122**, 016403 (2019).
- [7] D. C. Miller, S. D. Mahanti, and P. M. Duxbury, *Phys. Rev. B* **97**, 045133 (2018).
- [8] J. A. Wilson, *Phys. Rev. B* **17**, 3880 (1978).
- [9] B. Sipoš, F. Kusmartseva, A. Akrap, H. Berger, L. Forro, and E. Tutis, *Nat. Mater.* **7**, 960 (2008).
- [10] D. C. Freitas, P. Rodiere, M. R. Osorio, E. Navarro-Moratalla, N. M. Nemes, V. G. Tissen, L. Cario, E. Coronado, M. Garcia-Hernandez, S. Vieira, M. Nunez-Regueiro, and H. Suderow, *Phys. Rev. B* **93**, 184512 (2016).
- [11] P. Monceau, *Adv. Phys.* **61**, 325 (2012).
- [12] B. Wang, Y. Liu, K. Ishigaki, K. Matsubayashi, J. Cheng, W. Lu, Y. Sun, and Y. Uwatoko, *Phys. Rev. B* **95**, 220501(R) (2017).
- [13] J. Guo, H. Luo, H. Yang, L. Wei, H. Wang, W. Yi, Y. Zhou, Z. Wang, S. Cai, S. Zhang, X. Li, Y. Li, J. Liu, K. Yang, A. Li, J. Li, Q. Wu, R. J. Cava, and L. Sun, *arXiv:1704.08106v1*.
- [14] K. Cho, M. Konczykowski, S. Teknowijoyo, M. A. Tanatar, J. P. Guss, P. B. Gartin, J. M. Wilde, A. Kreyssig, R. J. McQueeney, A. I. Goldman, V. Mishra, P. J. Hirschfeld, and R. Prozorov, *Nat. Commun.* **9**, 2796 (2018).
- [15] C. Rovira and M. H. Whangbo, *Inorg. Chem.* **32**, 4094 (1993).
- [16] R. Huisman and F. Jellinek, *J. Less-Common Met.* **17**, 111 (1969).
- [17] M.-H. Whangbo and E. Canadell, *J. Am. Chem. Soc.* **114**, 9587 (1992).
- [18] B. E. Brown and D. J. Beentsen, *Acta Crystallogr.* **18**, 31 (1965).
- [19] S. van Smaalen, *Acta Crystallogr. A* **61**, 51 (2005).
- [20] R. Ang, Z.C. Wang, C.L. Chen, J. Tang, N. Liu, Y. Liu, W.J. Lu, Y. P. Sun, T. Mori, and Y. Ikuhara, *Nat. Commun.* **6**, 6091 (2015).
- [21] L. Liu, D. F. Shao, L. J. Li, W. J. Lu, X. D. Zhu, P. Tong, R. C. Xiao, L. S. Ling, C. Y. Xi, L. Pi, H. F. Tian, H. X. Yang, J. Q. Li, W. H. Song, X. B. Zhu, and Y. P. Sun, *Phys. Rev. B* **94**, 045131 (2016).
- [22] Sh. Qiao, X. Li, N. Wang, W. Ruan, C. Ye, P. Cai, Z. Hao, H. Yao, X. Chen, J. Wu, Y. Wang, and Z. Liu, *Phys. Rev. X* **7**, 041054 (2017).
- [23] H. Luo, W. Xie, J. Tao, H. Inoue, A. Gyenis, J. W. Krizan, A. Yazdani, Y. Zu, and R. J. Cava, *Proc. Natl. Acad. Sci U.S.A.* **112**, E1174 (2015).
- [24] L. Li, X. Deng, Z. wang, Y. liu, M. Abeykoon, E. Dooryhee, A. Tomic, Y. Huang, J. B. Warren, E. S. Bozin, S. J. L. Billinge, Y. Sun, Y. Zhu, G. Kotilar, and C. Petrovic, *NPJ Quantum Mater.* **2**, 11 (2017).
- [25] T. Egami and S. J. L. Billinge, *Underneath the Bragg Peaks: Structural Analysis of Complex Materials* (Pergamon, Oxford, UK, 2003).
- [26] V. Petkov, in *Characterization of Materials* (John Wiley & Sons, New York, 2003).
- [27] W. Wang, D. Dietzel, and A. Schirmeisen, *Sci. Rep.* **9**, 7066 (2019).
- [28] D. E. Moncton, J. D. Ake, and F. J. DiSalvo, *Phys. Rev. B* **16**, 801 (1977).
- [29] R. M. Fleming, D. E. Moncton, D. B. McWhan, and F. J. DiSalvo, *Phys. Rev. Lett.* **45**, 576 (1980).
- [30] T. Butz, S. Saibene, and A. Lerf, *J. Phys. C: Solid State Phys.* **19**, 2675 (1986).

- [31] R. Brower and F. Jellinek, *Physica B+C* **99**, 51 (1980).
- [32] V. Petkov, K. Chapagain, S. Shastri, and Y. Ren, *Phys. Rev. B* **101**, 121114(R) (2020).
- [33] T. Sorgel, J. Nuss, U. Wedig, R. K. Kremer, and M. Jansen, *Mater. Res. Bull.* **41**, 987 (2006).
- [34] A. Vernes, H. Ebert, W. Bensch, W. Heid, and C. Nather, *J. Phys.: Condens. Matter* **10**, 761 (1998).
- [35] M.-L. Doublet, S. Remy, and F. Lemoigno, *J. Chem. Phys.* **113**, 5879 (2000).
- [36] C. Ayache, R. Currat, B. Hennion, and P. Moline, *J. de Physique IV Colloque* **3**, C2-125 (1993).
- [37] A. M. Gabovich, A. I. Voitenko, J. F. Annett, and M. Ausloos, *Superconduct. Sci. Technol.* **14**, R1 (2001).
- [38] L.-L. Wei, S.-S. Sun, K. Sun, Y. Liu, D.-F. Shao, W.-J. Lu, Y.-P. Sun, H.-F. Tian, and H.-X. Yang, *Chin. Phys. Lett.* **34**, 086101 (2017).
- [39] B. H. Toby and R. B., and Von Dreele, *J. Appl. Crystallogr.* **46**, 544 (2013).
- [40] V. Petkov, *J. Appl. Crystallogr.* **22**, 387 (1989).
- [41] V. Petkov, S. D. Shastri, J.-W. Kim, Sh. Shiyao, J. Luo, J. Wu, and Ch.-J. Zhong, *Acta Crystallogr. A* **74**, 553 (2018).
- [42] Y. Waseda, *Novel Applications of Anomalous (Resonance) X-ray Scattering for Characterization of Disordered Materials* (Springer, Berlin, 1984).
- [43] V. Petkov, I.-K. Jeong, J. S. Chung, M. F. Thorpe, S. Kycia, and S. J. L. Billinge, *Phys. Rev. Lett.* **83**, 4089 (1999).
- [44] R. L. McGreevy and L. Pusztai, *Mol. Simul.* **1**, 359 (1988).
- [45] O. Gereben and V. Petkov, *J. Phys.: Condens. Matter* **25**, 454211 (2013).
- [46] See Supplemental Material at <http://link.aps.org/supplemental/10.1103/PhysRevB.102.134119> for additional modeling results.
- [47] F. Hulliger, in *Structural Chemistry of Layer-Type Phases*, edited by F. Levy (Reidel Publishing Co., Dordrecht, 1976).
- [48] M. Kertesz and R. Hoffmann, *J. Am. Chem. Soc.* **106**, 3453 (1984).
- [49] F. R. Gamble, *J. Solid State Chem.* **9**, 358 (1974).
- [50] T. Hibma, in *Intercalation Chemistry*, edited by M. S. Whittingham and A. J. Jacobson (Academic Press, New York, 1982), pp. 292–295.
- [51] H. Luo, W. Xie, E. M. Seibel, and R. J. Cava, *J. Phys.: Condens. Matter* **27**, 365701 (2015).
- [52] P.W. Anderson, *J. Phys. Chem. Solids.* **11**, 26 (1959).
- [53] H. Eisaki, N. Kaneko, D. L. Feng, A. Damascelli, P. K. Mang, K. M. Shen, Z.-X. Shen, and M. Greven, *Phys. Rev. B* **69**, 064512 (2004).
- [54] C. Brun, T. Cren, V. Cherkez, F. Debontridder, S. Pons, D. Fokin, M. C. Tringides, S. Bozhko, L.B. Ioffe, B. L. Altshuler, and D. Roditchev, *Nat. Phys.* **10**, 444 (2014).
- [55] Y. Wang, A. Kreisel, P. J. Hirschfeld, and V. Mishra, *Phys. Rev. B* **87**, 094504 (2013).
- [56] Z. R. Ye, Y. Zhang, F. Chen, M. Xu, J. Jiang, X. H. Niu, C. H. P. Wen, L. Y. Xing, X. C. Wang, C. Q. Jin, B. P. Xie, and D. L. Feng, *Phys. Rev. X* **4**, 031041 (2014).
- [57] H. Ryu, H. Lei, A. I. Frenkel, and C. Petrovic, *Phys. Rev. B* **85**, 224515 (2012).